

High-Discretization Method of Moments for Capacitance Calculation: A Cube and a Hollow Cylinder

Haiyong Gu,^{1,*} Liyuan Huang,^{1,†} Peide Yang,^{1,‡} and Tianshu Luo^{1,§}

¹*School of Information Science and Technology, Xiamen University Tan Kah Kee College, 363105 Zhangzhou, Fujian, China*

This paper employs the method of moments (MOM) to calculate the capacitances of a cube and a hollow cylinder. For the cube, each face was divided into a maximum of 600×600 sub-areas. By fully exploiting the geometric symmetry between sub-areas and incorporating parallel computing, computational resources were significantly conserved. Our results show that the calculated capacitance of the cube first increases and then decreases as the number of sub-areas increases. When each face was divided into 90×90 sub-areas, the capacitance of the unit cube (with an edge length of 1 m) reached a maximum reference value of 73.519014 pF. This indicates that higher accuracy cannot be achieved merely by indefinitely increasing the number of discretized sub-areas. Subsequently, the method was applied to compute the capacitance of a hollow cylinder. The results were compared with numerical solutions based on Lekner's theoretical formula and Cavendish's experimental values, showing good agreement among the three.

Keywords: Method of Moments, Capacitance, Cube, Hollow Cylinder

I. INTRODUCTION

The calculation of capacitance for a cube constitutes a classic challenge in electromagnetism, for which no analytical solution has been identified to date, and existing approaches rely exclusively on numerical methods. Polya [1] established the upper and lower bounds for the capacitance of a cube with edge length a : $0.62211a < C < 0.71055a$ cm. Reitan and Higgins [2] calculated its capacitance as $0.6555a$ cm by dividing each face of the cube into 6×6 sub-areas. Bai and Longren [3] employed a similar approach, dividing each face of the cube into a maximum of 20×20 sub-areas, and obtained a capacitance value of $0.6601a$ cm. This method was later developed into the method of moments. Sarkarati [4] applied the Method of Moments with analytically evaluated quadruple integrals, discretizing each face into 48×48 sub-areas, and obtained a capacitance value of $0.66047a$ cm. Zhou and Szabo [5] obtained a capacitance value of $0.6632a$ cm using the Brownian dynamics algorithm. Hwang [6] obtained a capacitance value of $0.66067813a$ cm using the refined Brownian dynamics algorithm. Read [7] calculated a capacitance value of $0.6606785a$ cm using the modified Boundary Element Method. Brown [8] obtained a capacitance value of $0.661a$ cm using the finite difference method. Helsing and Perfekt [9] employed an efficient boundary integral equation solver based on kernel splitting and recursive compression, and obtained a capacitance value of $0.66067815a$ cm for the unit cube.

In Sec. II, we employ the method of moments to discretize each face of a cube. Our approach utilizes both even and odd partitions, and by exploiting the symmetry among the resulting sub-areas, we achieve a maximum discretization of 600×600 sub-areas per face. The computational efficiency is significantly enhanced through parallel computing implemented in Python code, leading to a substantial saving of computational resources. In Sec. III, we apply this method of moments to calculate the capacitance of hollow cylinders with arbitrary dimensions. Readers interested solely in the capacitance analysis of hollow cylinders may proceed directly to Sec. III without loss of continuity. The discussion and conclusions are presented in Sec. IV. Details of this study are listed in Apps. A- D.

All models and calculations in this study use SI units. The capacitance values cited from historical literature in Sec. I are originally in the CGS unit of centimeters. To ensure consistency, these values were converted to farads using the relation $1 \text{ cm (CGS)} \approx 1.1126 \times 10^{-12} \text{ F}$. For clarity, results are primarily presented in picofarads ($1 \text{ pF} = 10^{-12} \text{ F}$), with the original centimeter values provided in parentheses or captions where necessary.

II. CAPACITANCE OF A CUBE

In the method of moments, as illustrated in Fig. 1, each face of the cube is divided into 7×7 sub-areas (1 m Side Length). Due to symmetry considerations, these 49 sub-areas are classified into ten distinct categories labeled by numbers 1, 2, 3 \dots 10. Assuming that the charge carried by each sub-area is concentrated at its geometric center, the electric potential generated by a sub-area's own charge at its center can

* haiyong@xujc.com

† lyhuang@xujc.com

‡ yangpd@xujc.com

§ penny678@xujc.com

be determined through integration (A1), yielding a value of $3.52549\sigma/(4\pi\epsilon_0)$. The potential at this center arising from other sub-areas is approximated by $\sigma/(4\pi\epsilon_0d)$ (A2), where d is the distance between sub-area centers and σ is the charge density. By computing the cumulative electric potential at the center arising from all sub-areas, we derive the following equation:

$$\phi = \mathbf{P}\boldsymbol{\sigma} \quad (1)$$

where

- $\phi = (\phi_1, \phi_2, \dots, \phi_{10})^T$ is the column vector of surface electric potentials,
- $\boldsymbol{\sigma} = (\sigma_1, \sigma_2, \dots, \sigma_{10})^T$ is the column vector of surface charge densities, and
- \mathbf{P} is a 10×10 coefficient matrix. The full set of matrix elements P_{ij} is provided in App. B.

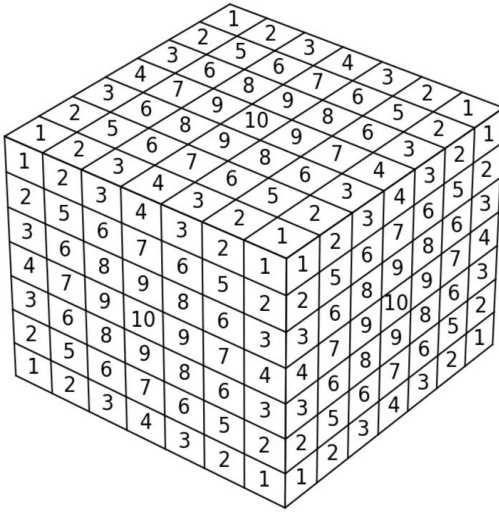


FIG. 1: Cube with Each Face Divided into 7×7 Sub-areas (1 m Side Length).

Based on the condition of electrostatic equilibrium, which requires the electric potentials to be equal, i.e., $\phi_1 = \phi_2 = \phi_3 = \phi_4 = \phi_5 = \phi_6 = \phi_7 = \phi_8 = \phi_9 = \phi_{10} = \phi = 1$ V, we solve to obtain:

$$\begin{aligned} \sigma_1 &= 3.117226765 \times 10^{-12}, & \sigma_6 &= 1.258597167 \times 10^{-12}, \\ \sigma_2 &= 2.200973724 \times 10^{-12}, & \sigma_7 &= 1.228313337 \times 10^{-12}, \\ \sigma_3 &= 2.059951977 \times 10^{-12}, & \sigma_8 &= 1.155954786 \times 10^{-12}, \\ \sigma_4 &= 2.016716775 \times 10^{-12}, & \sigma_9 &= 1.125280939 \times 10^{-12}, \\ \sigma_5 &= 1.357289047 \times 10^{-12}, & \sigma_{10} &= 1.094506278 \times 10^{-12}. \end{aligned} \quad (2)$$

Therefore, the total charge Q can be derived:

$$\begin{aligned} Q &= 24\sigma_1 + 48\sigma_2 + 48\sigma_3 + 24\sigma_4 + 24\sigma_5 \\ &\quad + 48\sigma_6 + 24\sigma_7 + 24\sigma_8 + 24\sigma_9 + 6\sigma_{10} \\ &= 5.11522896 \times 10^{-10} \text{ C} \end{aligned} \quad (3)$$

According to the electrostatic theorem that the capacitances of geometrically similar solids are proportional to their corresponding linear dimensions, the capacitance C of a cube with edge length a m is given by:

$$C = \frac{Q}{\phi} = 73.074699a \text{ pF} \quad (4)$$

Unlike the method of D. K. Reitan and T. J. Higgins [2], which employed only even-numbered divisions of the cube's surface (up to a maximum of 6×6 square sub-areas per face), our approach incorporates both even and odd divisions. Although the subsequent work by Er-Wei Bai and Karl E. Lonngren [3] extended the partitioning scheme to include odd divisions (up to 20×20 sub-areas per face), it did not account for the geometric symmetry among the resulting sub-areas. As illustrated in Fig. 1, even under odd-numbered divisions, the sub-areas on the cube's surface retain inherent symmetries, allowing them to be systematically classified. In the subsequent calculations, we explicitly utilize this symmetry, which substantially reduces computational resource requirements.

We divided each face of the cube into 7×7 , 10×10 , 20×20 , up to a maximum of 600×600 sub-areas. The calculations showed that the capacitance reached a maximum value of $73.519014a$ pF when each face was divided into 90×90 sub-areas. As the number of divisions increased beyond this point, the calculated capacitance gradually decreased, as shown in Fig. 2. Detailed capacitance values are provided in Table V of App. C.

The initial increase in capacitance can be explained using Thomson's theorem, which Maxwell first employed to estimate the capacitance of finite-length cylinder [10]. Thomson's theorem tells us that when a conductor reaches electrostatic equilibrium, its electrostatic field energy is minimized. The expressions for the electrostatic field energy W and the total charge Q can be written as follows

$$\begin{aligned} W &= \frac{1}{2} \int \phi(\xi) \sigma(\xi) dS \\ Q &= \int \sigma(\xi) dS \end{aligned} \quad (5)$$

Specifically, when the conductor reaches electrostatic equilibrium, its electrostatic field energy W_0 can be expressed as

$$W_0 = \frac{1}{2} \phi_0 Q = \frac{1}{2} \frac{Q}{C} Q = \frac{1}{2} \frac{Q^2}{C} \quad (6)$$

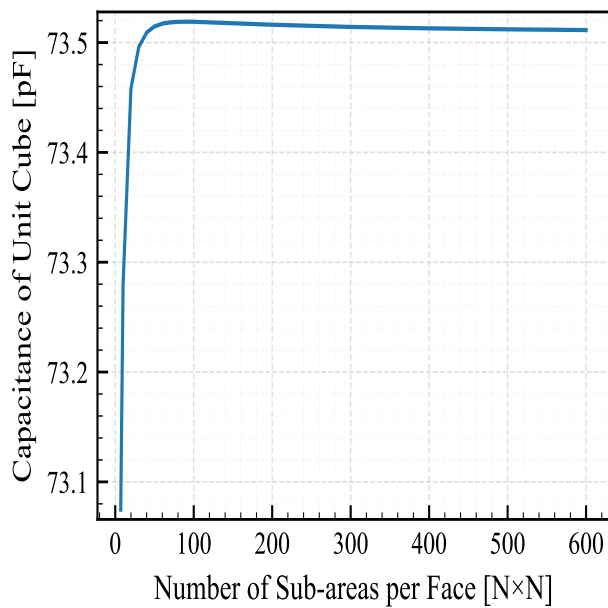


FIG. 2: Capacitance of a Unit Cube (edge length: 1 m) with Each Face Divided into $N \times N$ Sub-areas (N : X-Axis).

Hence,

$$C = \frac{Q^2}{2W_0} \quad (7)$$

According to Thomson's theorem, the electrostatic field energy W for any charge distribution satisfies $W \geq W_0$. Consequently,

$$C = \frac{Q^2}{2W_0} \geq \frac{Q^2}{2W} \quad (8)$$

As the number of sub-areas increases, the charge distribution on the cube surface progressively approaches electrostatic equilibrium, i.e., W approaches W_0 more closely, resulting in a gradual increase in capacitance.

The observed reduction in capacitance in the unit cube arises from errors due to discretization. As the number of subdivisions on each face of the cube increases, this error becomes the dominant effect. The specific and detailed reason likely stems from the potential approximation in formula (A2). It generally overestimates the electric potential, as the potential in each sub-area is fixed at 1 V, which results in an underestimated charge density and thereby leads to a reduced capacitance. A more detailed analysis can be found in App. D. This poses a challenge to the Method of Moments, as it dictates that the error introduced by discretization prevents us from obtaining the exact value of a cube's capacitance, even with an infinite increase in the number of sub-areas.

The comparison between our calculated results and those obtained by other methods is presented in Table I. As shown

in the table, when discretizing the cube surface using the method of moments, the capacitance obtained with 90×90 discretization is higher than that calculated with 6×6 , 20×20 , and 48×48 discretization. In addition, the cube capacitance calculated in this paper with 90×90 discretization is lower than the results obtained using the Brownian dynamics algorithm [5] and the finite difference method [8]. Since discretization errors usually lead to underestimation of capacitance, combined with the trend shown in Fig. 2, the peak value obtained in this analysis—the result of 90×90 discretization—is selected as the reference. Therefore, it can be inferred that the actual capacitance of the cube with an edge length of 1 m should be higher than the 90×90 discretization result of 73.519014 pF.

Theoretical Method	Results [pF] (Original [cm])
Method of Moments (6×6) [2]	72.930930 (0.6555)
Method of Moments (20×20) [3]	73.442726 (0.6601)
Method of Moments (48×48) [4]	73.483892 (0.66047)
Brownian dynamics algorithm [5]	73.787632 (0.6632)
Refined Brownian dynamics algorithm [6]	73.507049 (0.66067813)
Boundary element method [7]	73.507980 (0.6606785)
Finite difference method [8]	73.542860 (0.661)
Boundary integral equation solver [9]	73.507051(0.66067815)
our result (90×90)	73.519014

TABLE I: Capacitance Values of a Unit Cube (edge length: 1 m) Computed with Different Numerical Methods (Values in parentheses are the original data from the literature).

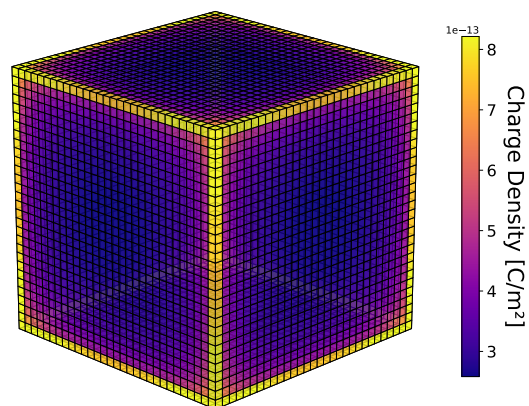


FIG. 3: Surface Charge Density Distribution on a Cube (edge length: 1 m) with Each Face Divided into 30×30 Sub-areas.

Fig. 3 shows the surface charge density distribution for a cube with each face divided into 30×30 sub-areas. The charge density is highest at the cube's vertices. It gradually decreases along the edges from the vertices toward the mid-points of the edges and attains its minimum at the center of each face. This behavior is consistent with the conclusions derived from electrostatic principles.

III. CAPACITANCE OF A CYLINDER

The capacitance of finite-length cylinders, as another classic electrostatic problem lacking an analytical solution, has been extensively investigated through numerical methods in numerous studies. Cavendish first experimentally measured the capacitance of cylinder, and later Maxwell provided the theoretical formulation for this configuration [10].

For a hollow cylinder of length L and radius R : When $L \gg R$, Maxwell derived the lower bound for the capacitance as $\frac{1/2L}{\ln \frac{2L}{R} - 1}$. When $L \ll R$, the hollow cylinder reduces to a circular ring. Refs. [11–14] indicate that the capacitance C approaches $\frac{\pi R}{\ln(32R/L)}$. Meanwhile, Landau [15] calculated the capacitance of a thin ring through an elegant integral method, yielding $\frac{\pi R}{\ln \frac{16R}{L}}$.

For a closed cylinder, when the length is much smaller than the radius ($L \ll R$), the cylinder reduces to a disk. Maxwell's theoretical approximation $\frac{2}{\pi} \left(R + \frac{L}{4\pi} \ln \frac{2R}{L} \right)$ coincides with the capacitance of a disk derived by Landau from an ellipsoidal conductor [15].

Ref. [13, 14, 16–18] present theoretical derivations for the capacitance of the hollow cylinder with other L/R ratios, while Ref. [17, 18] additionally provide the charge density distribution on the surface of the cylinder. For the capacitance of a hollow cylinder with arbitrary ratios of L/R , de Sousa [19] provided numerical solutions across the full range of aspect ratios, while Paffuti [20] computed capacitances for cylinders over an extensive range of aspect ratios using a Galerkin method. Lekner [21] proposed the following theoretical formula:

$$\begin{pmatrix} K_{00} & K_{01} & \cdots & K_{0\infty} \\ K_{10} & K_{11} & \cdots & K_{1\infty} \\ \vdots & \vdots & \ddots & \vdots \\ K_{m0} & \cdots & \cdots & K_{m\infty} \end{pmatrix} \begin{pmatrix} C_0 \\ C_1 \\ \vdots \\ C_\infty \end{pmatrix} = \begin{pmatrix} 1 \\ 0 \\ \vdots \\ 0 \end{pmatrix} \quad (9)$$

Here, C_0 denotes the capacitance of the cylinder. The matrix elements K_{mn} can be expressed via the Meijer G-function [22].

In Mathematica notation, K_{mn} is written as:

$$K_{mn} = \frac{(-1)^{m+n}}{4\pi^3 \epsilon_0 L} G \left(\left(\left[\left[\frac{1}{2} - m - n, \frac{1}{2} - |m - n| \right], \left[\frac{1}{2} + |m - n|, \frac{1}{2} + m + n \right], \left[[0, 0, 0], [0], \frac{R^2}{4L^2} \right] \right] \right) \right) \quad (10)$$

Premultiplying both sides of Eq.(9) by the inverse matrix of K_{mn} yields:

$$\begin{pmatrix} C_0 \\ C_1 \\ \vdots \\ C_\infty \end{pmatrix} = \begin{pmatrix} K_{00} & K_{01} & \cdots & K_{0\infty} \\ K_{10} & K_{11} & \cdots & K_{1\infty} \\ \vdots & \vdots & \ddots & \vdots \\ K_{m0} & \cdots & \cdots & K_{m\infty} \end{pmatrix}^{-1} \begin{pmatrix} 1 \\ 0 \\ \vdots \\ 0 \end{pmatrix} \quad (11)$$

Therefore, the capacitance C_0 of the cylinder capacitance can be derived

$$C_0 = L_{00} \quad (12)$$

L_{00} is the first matrix element of the inverse matrix of K_{mn} . The capacitance for a hollow cylinder with any aspect ratio L/R can then be computed by truncating this infinite matrix. If the reader is interested in a more detailed derivation, they are referred to Ref. [21].

Following the method for calculating the capacitance of a cube, we applied the method of moments to determine the capacitance of a hollow cylinder. In Ref. [23], the capacitance was estimated by subdividing a 1-meter-long hollow cylinder into ten annular rings. In this article, we not only increased the number of annular rings dividing the hollow cylinder but also further subdivided each ring into square sub-areas. By exploiting its axial symmetry, the surface of the hollow cylinder is divided into L annular rings with a width of 1 m, each of which is further subdivided into K square sub-areas with side lengths of 1 m, as illustrated in Fig. 4. The electric potential at the center of a sub-area generated by its own charge is $3.52549\sigma/(4\pi\epsilon_0)$ (A1), while contributions from other sub-areas are $\sigma/(4\pi\epsilon_0 d)$ (A2), where σ is the charge density and d the center-to-center distance between sub-areas. Thus, the electric potential of an annular ring generated by its own charge can be expressed as a summation:

$$\sum_{n=1}^{K-1} \frac{\pi\sigma}{4\pi\epsilon_0 K \sin \frac{n\pi}{K}} + \frac{3.52549\sigma}{4\pi\epsilon_0} \quad (13)$$

Here, K is also the circumference of the annular ring. The electric potential generated by one annular ring at another can be derived as

$$\sum_{n=0}^{K-1} \frac{\sigma}{4\pi\epsilon_0 \left(d^2 + \frac{K^2}{\pi^2} \sin^2 \left(\frac{n\pi}{K} \right) \right)^{\frac{1}{2}}} \quad (14)$$

d denotes the distance between the centers of the two annular rings.

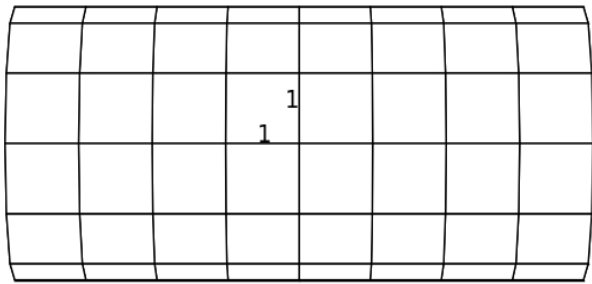


FIG. 4: The surface of a hollow cylinder is divided into L annular rings of 1 m width, each subdivided into K square sub-areas with 1 m side length.

Setting the electric potential of every annular ring to 1 V allows us to solve for the surface charge density σ . The capacitance is then obtained directly from the total charge. For geometrically similar cylindrical configurations, the ratio of capacitance to cylinder radius R remains constant. We computed this capacitance-to-radius ratio for different L/K values and compared the results with Lekner's [21] numerical calculations, as summarized in Table II.

q/m	our results (C/R)	Lekner ($N = 6$) (C/R)
1000/94248	56.6181	56.6184 (0.508884)
1000/31416	68.8969	68.8973 (0.619246)
5000/47124	90.5870	90.5869 (0.814191)
5000/31416	101.4889	101.4888 (0.912177)
5000/23562	111.0306	111.0305 (0.997937)
5000/15708	127.9917	127.9915 (1.150382)
5000/7854	171.1675	171.1671 (1.538442)
5000/5236	208.7809	208.7801 (1.876506)
5000/1571	421.5004	421.5266 (3.788663)
5000/524	900.2549	900.6987 (8.095440)

TABLE II: Comparison of Capacitance-to-Radius Ratios C/R [pF/m] for Hollow Cylinders at Different L/K Ratios: Our Numerical Results vs Lekner's Truncated Matrix Method (6th-Order) [21]. Lekner's original values are shown in parentheses. L : Cylinder Length [m]; K : Base Circumference [m]; R : Radius ($R = K/2\pi$).

It can be observed that our numerical results for the hollow cylinder capacitance show excellent agreement with Lekner's data. However, slightly larger discrepancies were observed in the L/K ratios of 5000/1571 and 5000/524, mainly due to the limited computational resources that restricted the maximum value of L to 5000, while the smaller values of K resulted in

increased errors.

Our numerical results for the hollow cylinder capacitance are compared with Lekner's calculations and Cavendish's experimental measurements in Table III. In our computations, the parameters L and K were assigned scaled-up integer values through proportional amplification. Our numerical results show good agreement with those calculated using Eq.(12) derived by Lekner, while exhibiting a relatively larger discrepancy when compared to Cavendish's experimental measurements. This discrepancy can be attributed not only to the errors inherent in the theoretical calculations but also to the measurement errors associated with Cavendish's experiment itself. A review of the original notes detailing his experimental procedures reveals that, constrained by the technological limitations of the time, several factors contributed to the experimental uncertainty. These included visual judgment errors in reading the pith-ball electrometer, charge leakage, and imperfect insulation, as documented in his records [10].

L	K	our results	Lekner ($N = 6$)	measured by Cavendish
1.3767	0.0583	16.5876	16.5893	16.2609(5.754)
0.9119	0.2019	17.0711	17.0712	17.0804(6.044)

TABLE III: Comparison of Hollow Cylinder Capacitance Values [pF] (Numerical Solutions(This Work), Lekner's [21] 6th-Order Matrix Truncation Solutions, and Cavendish's Experimental Data [10] with Length L and base circumference K in Meters. original values in inches from Cavendish's measurements are given in parentheses).

As shown in Fig. 5, the charge density distribution of the hollow cylinder exhibits higher values at both ends and lower values in the central region, with sharp variations at the ends and gradual variations in the middle, which is consistent with theoretical expectations.

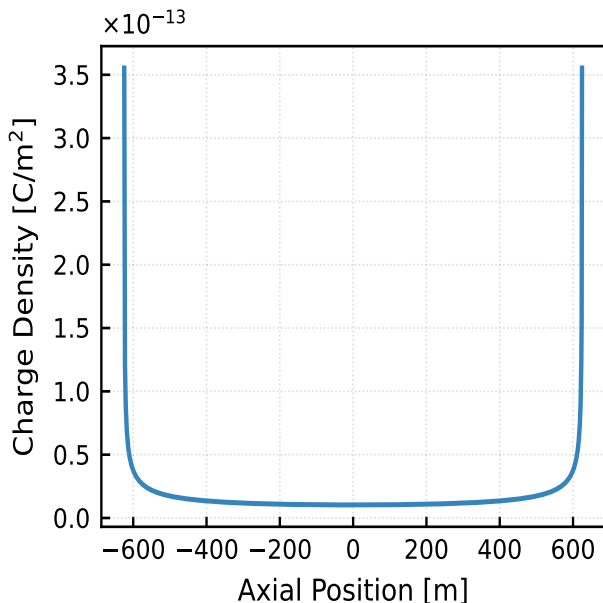


FIG. 5: The Charge Density Distribution Curve of the Hollow Cylinder with Length $L = 1250$ m and Base Circumference $K = 3927$ m (Diameter $D = 1250$ m).

IV. DISCUSSION AND CONCLUSION

This study extends the sub-areas method proposed by D. K. Reitan and T. J. Higgins for calculating cube capacitance, which later evolved into the method of moments. Reitan and Higgins only employed even divisions of the cube's surface, with a maximum partition scale of 6×6 square sub-areas per face. Building on this, the work of Er-Wei Bai and Karl E. Lonngren incorporated both even and odd divisions; however, they did not exploit the symmetry among the sub-areas on the cube's faces. Their maximum partition scale was 20×20 sub-areas per face.

It is worth noting that geometric symmetries among the sub-areas on the cube's surface still exist even under odd divisions. The present research retains these symmetries fully while being compatible with both even and odd divisions, thereby significantly reducing computational resource requirements. We have increased the maximum partition scale on each face of the cube to 600×600 sub-areas.

Based on the described method, a Python program utilizing a parallel computing architecture was developed and is available from the authors upon request. The computation for a 600×600 partition scale takes approximately 1 hour and 43 minutes on a desktop equipped with an 8-core 11th-generation Intel i7 processor.

We find that the computed capacitance of a unit cube (edge length: 1 m) does not converge monotonically with finer discretization. Instead, it first increases, peaks at 73.519014 pF

for 90×90 sub-areas per face, and then gradually decreases. We introduced Thomson's theorem to explain the initial rise in capacitance. In the early stage, as the number of sub-areas on each face of the cube increases, the surface charge distribution gradually approaches electrostatic equilibrium, leading to a reduction in electrostatic energy. According to Eq.(8), the capacitance correspondingly increases and converges toward the theoretical value. However, upon further refinement, errors inherent in the discretization scheme itself become dominant, causing the calculated capacitance to decrease. Through a detailed analysis based on rigorous integral calculations, we find that the potential approximation formula (A2) systematically overestimates the actual potential. This results in an underestimated charge density from the inversion process, and consequently leads to an underestimated capacitance. This error becomes dominant under fine discretization, posing a challenge to the method of moments in such problems: even with an unlimited increase in sub-areas, discretization-induced errors may still prevent the numerical results from converging to the exact value. Finally, we have visualized the charge density distribution on the surface of the cube, as presented in Fig. 3. This distribution pattern is consistent with the predictions of electrostatic theory.

Subsequently, this method was applied to calculate the capacitance of a hollow cylinder. The cylinder was divided into L annular rings (1 m in width), each subdivided into K square sub-areas (1 m side length). We derived analytical expressions for self-potential (Eq.(13)) and mutual-potential (Eq.(14)) between ring elements. For various L/K ratios, our computed capacitances show excellent agreement with Lekner's numerical solutions and are also consistent with Cavendish's experimental measurements. Furthermore, the Python code developed in this paper for calculating hollow cylinder capacitance is highly efficient. For the slowest case, L/K (5000:47124), using parallel computing on a desktop with an 8-core 11th-generation Intel i7 processor, a single run takes only 891 seconds. For the fastest case, L/K (1000:31416), it takes just 7 seconds, demonstrating excellent numerical performance. In addition, we present the charge density distribution along the axial direction for a hollow cylinder with an aspect ratio of 1, as shown in Fig. 5. Its variation trend is consistent with the predictions of electrostatic theory.

ACKNOWLEDGMENTS

We would like to express our gratitude to Zhidao Bu for his significant assistance in literature retrieval.

DECLARATIONS

H.G. is supported by the Fujian Provincial Education and Scientific Research Program for Young and Middle-aged Teachers (Science & Technology Category) under Grant No. JAT231183. P.Y. is supported by the Fujian Provincial Education and Scientific Research Program for Young and Middle-aged Teachers (Science & Technology Category) under Grant No. JZ230071.

Appendix A: Electric Potential at the Center and in the Exterior Region of a Unit Square

Assuming a square with a side length of 1 m as shown in Fig. 6, where the charge density σ is uniformly distributed, the electric potential at the center of the square can be expressed as [24]

$$\begin{aligned}\phi &= \frac{4\sigma}{4\pi\epsilon_0} \int_0^{\frac{1}{2}} \int_0^{\frac{1}{2}} \frac{dx dy}{(x^2 + y^2)^{\frac{1}{2}}} = \frac{4\sigma}{4\pi\epsilon_0} \int_0^{\frac{1}{2}} \sinh^{-1} \frac{1}{2y} dy \\ &= \frac{2\sigma}{4\pi\epsilon_0} \int_1^{\infty} u^{-2} \sinh^{-1} u du = \frac{4\sigma}{4\pi\epsilon_0} \ln[1 + (2)^{\frac{1}{2}}] \\ &= \frac{3.52549\sigma}{4\pi\epsilon_0}\end{aligned}\quad (\text{A1})$$

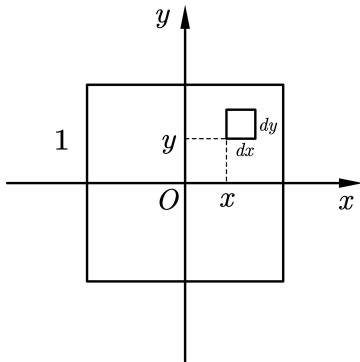


FIG. 6: Schematic diagram of the electric potential calculation at the center of a unit square.

When point O is located outside the square at a distance d from its center, as shown in Fig. 7, the electric potential can

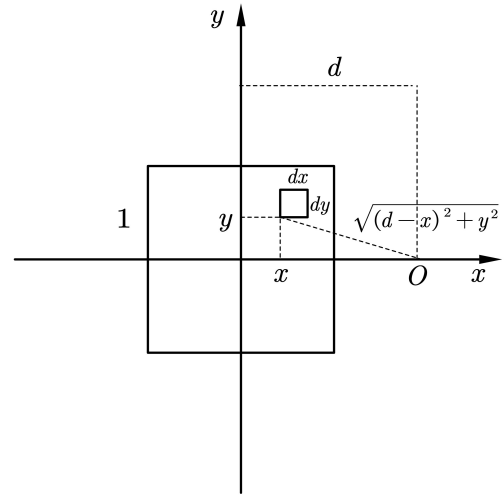


FIG. 7: Schematic diagram of the electric potential calculation at a distance d ($d > 1$) from the center of a unit square.

be expressed as [24]

$$\phi = \frac{\sigma}{4\pi\epsilon_0} \int_{-\frac{1}{2}}^{\frac{1}{2}} \int_{-\frac{1}{2}}^{\frac{1}{2}} \frac{dx dy}{\sqrt{(d-x)^2 + y^2}} \sim \frac{\sigma}{4\pi\epsilon_0 d} \quad (\text{A2})$$

Appendix B: Coefficient Matrix \mathbf{P}

The coefficient matrix \mathbf{P} from the main matrix Eq.(1) is given below. The element P_{ij} in the i -th row and j -th column corresponds to the coefficient of σ_j in the equation for ϕ_i .

$i \setminus j$	1	2	3	4	5	6	7	8	9	10
1	9.052	10.581	8.743	4.181	4.760	8.685	4.222	4.232	4.184	1.040
2	5.290	13.204	9.773	4.553	5.235	9.520	4.597	4.600	4.539	1.127
3	4.371	9.773	13.117	5.398	4.959	10.215	5.066	4.881	4.845	1.199
4	4.181	9.106	10.796	8.515	4.778	10.223	5.473	4.975	4.981	1.228
5	4.760	10.470	9.919	4.778	7.851	10.748	5.015	5.155	5.017	1.244
6	4.342	9.520	10.215	5.111	5.374	13.384	5.637	5.726	5.549	1.365
7	4.222	9.195	10.132	5.473	5.015	11.274	8.200	5.744	5.938	1.428
8	4.232	9.199	9.762	4.975	5.155	11.451	5.744	8.603	6.635	1.646
9	4.184	9.078	9.690	4.981	5.017	11.098	5.938	6.635	9.204	1.945
10	4.161	9.015	9.590	4.914	4.977	10.922	5.712	6.582	7.782	4.476

TABLE IV: Complete elements of the 10×10 coefficient matrix \mathbf{P} . Note: The elements of this coefficient matrix need to be divided by $4\pi\epsilon_0$.

Appendix C: Capacitance of a Unit Cube

Number of Sub-areas	Results [pF]
7 × 7	73.074699
10 × 10	73.280263
20 × 20	73.458128
30 × 30	73.496007
40 × 40	73.509142
50 × 50	73.514687
60 × 60	73.517232
70 × 70	73.518406
80 × 80	73.518892
85 × 85	73.518986
89 × 89	73.519013
90 × 90	73.519014
91 × 91	73.519013
95 × 95	73.518991
100 × 100	73.518934
200 × 200	73.516239
300 × 300	73.514237
400 × 400	73.512946
500 × 500	73.512054
600 × 600	73.511405

TABLE V: Calculated Capacitance Values for a Unit Cube (edge length: 1 m) with Each Face Divided into Varying Numbers of Sub-areas.

Appendix D: Discretization Error Analysis

Taking the center of a cube face as the origin (e.g., the center of the sub-area marked 10 in Fig. 1), the electric potential it produces at other target sub-areas on the cube surfaces is calculated. The difference between the results from the full integral expression and the approximate formula (both given in formula (A2)) is analyzed. Three cases are examined separately:

- When the two sub-areas are coplanar, the potential difference $\Delta\phi$ is given by the following expression, where x_1 and y_1 are the coordinates of the center of the target sub-area. We define

$\mathbf{r} = (x_1, y_1, 0)$ and $\mathbf{r}' = (x, y, 0)$.

$$\begin{aligned}
\Delta\phi &= \frac{\sigma}{4\pi\epsilon_0} \left[\frac{1}{\sqrt{x_1^2 + y_1^2}} - \int_{-1/2}^{1/2} \int_{-1/2}^{1/2} \frac{dxdy}{\sqrt{(x_1 - x)^2 + (y_1 - y)^2}} \right] \\
&= \frac{\sigma}{4\pi\epsilon_0} \left(\frac{1}{r} - \int_{-1/2}^{1/2} \int_{-1/2}^{1/2} \frac{dxdy}{|\mathbf{r} - \mathbf{r}'|} \right), \quad r = \sqrt{x_1^2 + y_1^2} \\
&= \frac{\sigma}{4\pi\epsilon_0} \left\{ \frac{1}{r} - \int_{-1/2}^{1/2} \int_{-1/2}^{1/2} dxdy \left[\frac{1}{r} + \frac{\mathbf{r} \cdot \mathbf{r}'}{r^3} \right. \right. \\
&\quad \left. \left. + \frac{1}{2} \left(\frac{3(\mathbf{r} \cdot \mathbf{r}')^2}{r^5} - \frac{|\mathbf{r}'|^2}{r^3} \right) + \dots \right] \right\} \\
&= \frac{\sigma}{4\pi\epsilon_0} \left\{ \frac{1}{r} - \left[\frac{1}{r} + \frac{1}{24r^3} + O\left(\frac{1}{r^5}\right) \right] \right\} \\
&= \frac{\sigma}{4\pi\epsilon_0} \left[-\frac{1}{24r^3} + O\left(\frac{1}{r^5}\right) \right] < 0
\end{aligned} \tag{D1}$$

It can be observed that when two sub-areas are coplanar, the potential value yielded by the approximate formula (A2) is consistently lower than that obtained via two-dimensional integration, regardless of their separation distance.

- When the two sub-areas are on opposite faces, the potential difference $\Delta\phi$ is given by the following expression, where z_1 equals the edge length of the cube. Moreover, since the coordinate origin is located at the center of the face, we have $x_1, y_1 < z_1/2$. Hence, for this configuration, the potential calculated using the approximate formula (A2) is greater than that obtained through integration (Note that here we have only considered the potential generated by a sub-area at the center of a cube face on its opposite face).

$$\begin{aligned}
\Delta\phi &= \frac{\sigma}{4\pi\epsilon_0} \left[\frac{1}{\sqrt{x_1^2 + y_1^2 + z_1^2}} \right. \\
&\quad \left. - \int_{-1/2}^{1/2} \int_{-1/2}^{1/2} \frac{dxdy}{\sqrt{(x_1 - x)^2 + (y_1 - y)^2 + z_1^2}} \right] \\
&\approx \frac{\sigma}{4\pi\epsilon_0} \left[\frac{1}{r_0} - \left(\frac{1}{r_0} + \frac{x_1^2 + y_1^2}{8r_0^5} - \frac{1}{12r_0^3} \right) \right] \\
&\approx \frac{\sigma}{4\pi\epsilon_0} \cdot \frac{2z_1^2 - (x_1^2 + y_1^2)}{24r_0^5} > 0, \quad r_0 = \sqrt{x_1^2 + y_1^2 + z_1^2}
\end{aligned} \tag{D2}$$

- When the two sub-areas are on adjacent faces, the potential difference $\Delta\phi$ is given by the following expression, where x_1

equals half the edge length of the cube.

$$\begin{aligned} \Delta\phi &= \frac{\sigma}{4\pi\epsilon_0} \left[\frac{1}{\sqrt{x_1^2 + y_1^2 + z_1^2}} \right. \\ &\quad \left. - \int_{-1/2}^{1/2} \int_{-1/2}^{1/2} \frac{dxdy}{\sqrt{(x_1 - x)^2 + (y_1 - y)^2 + z_1^2}} \right] \quad (D3) \\ &\approx \frac{\sigma}{4\pi\epsilon_0} \left[\frac{1}{r_0} - \left(\frac{1}{r_0} + \frac{x_1^2 + y_1^2}{8r_0^5} - \frac{1}{12r_0^3} \right) \right] \\ &\approx \frac{\sigma}{4\pi\epsilon_0} \cdot \frac{2z_1^2 - (x_1^2 + y_1^2)}{24r_0^5}, \quad r_0 = \sqrt{x_1^2 + y_1^2 + z_1^2} \end{aligned}$$

Here, the sign of the electric potential difference $\Delta\phi$ depends on the values of x_1 , y_1 , and z_1 . We performed numerical calculations to determine the proportion of cases where $\Delta\phi$ takes positive values when the cube is divided into different numbers of sub-areas. The results are presented in Fig.8.

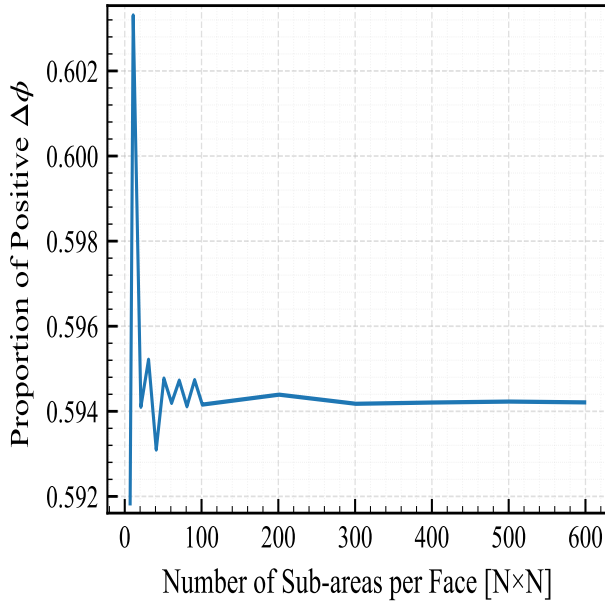


FIG. 8: Proportion of Positive $\Delta\phi$ with Each Face Divided into $N \times N$ Sub-areas (N : X-Axis).

From the Fig.8, it can be observed that the proportion of positive $\Delta\phi$ values remains essentially constant at approximately 59%, showing no significant dependence on the number of sub-areas used in the discretization. However, as the total number of sub-areas, $6 \times N^2$, increases, the difference between the number of sub-areas where $\Delta\phi$ takes positive values and those where it takes negative values also increases, meaning that the overestimation effect on the electric potential is enhanced. Considering that the cube possesses four adjacent faces and by synthesizing the two scenarios discussed above, we can draw a general conclusion: the electric potential calculated using the approximate formula (A2) is systematically

higher than the value obtained from the exact integral expression.

Since the potential for each sub-area is fixed at 1 V, this systematic overestimation leads to an underestimation of the computed charge density, which in turn results in a reduced capacitance value. As the number of sub-areas per cube face increases, the positive effect of finer discretization on enhancing the capacitance calculation becomes negligible. Beyond this point, the error inherent in the adopted potential approximation emerges as the dominant factor governing the result.

-
- [1] G. Pólya, *The American Mathematical Monthly* **54**, 201 (1947).
- [2] D. K. Reitan and T. J. Higgins, *Journal of applied Physics* **22**, 223 (1951).
- [3] E.-W. Bai and K. E. Lonngren, *Computers & Electrical Engineering* **28**, 317 (2002).
- [4] S. Sarkarati, M. M. Tehranchi, and E. Mehrshahi, “Precise calculation of electrical capacitance by means of quadruple integrals in method of moments technique,” (2022), arXiv:2206.04795 [cs.CE].
- [5] H.-X. Zhou, A. Szabo, J. F. Douglas, and J. B. Hubbard, *The Journal of chemical physics* **100**, 3821 (1994).
- [6] C.-O. Hwang, M. Mascagni, and T. Won, *Mathematics and Computers in Simulation* **80**, 1089 (2010).
- [7] F. H. Read, *Journal of Computational Physics* **133**, 1 (1997).
- [8] C. Brown, *Computers & Mathematics with Applications* **20**, 43 (1990).
- [9] J. Helsing and K.-M. Perfekt, “On the polarizability and capacitance of the cube,” (2012), arXiv:1203.5997 [physics.comp-ph].
- [10] H. Cavendish, *The Electrical Researches.. Henry Cavendish* (University Press, 1879).
- [11] R. W. Scharstein, *Journal of Electrostatics* **65**, 21 (2007).
- [12] C. M. Butler, *Journal of Applied Physics* **51**, 5607 (1980).
- [13] L. Verolino, *Electrical engineering (Berlin)* **78**, 201 (1995).
- [14] N. Lebedev and I. Skal’Skaya, *Soviet Physics Technical Physics* **18**, 28 (1973).
- [15] L. D. Landau, J. S. Bell, M. Kearsley, L. Pitaevskii, E. Lifshitz, and J. Sykes, *Electrodynamics of continuous media*, Vol. 8 (elsevier, Germany, 2013).
- [16] W. Smythe, *Journal of Applied Physics* **27**, 917 (1956).
- [17] J. D. Jackson, *American Journal of Physics* **68**, 789 (2000).
- [18] L. Vainshtein, *Soviet Physics-Technical Physics* **7**, 861 (1963).
- [19] J. R. de Sousa, “Electrostatics of a finite conducting cylinder: Elliptic-kernel integral equation and capacitance asymptotics,” (2025), arXiv:2601.00031 [physics.class-ph].
- [20] G. Paffuti, “Results for capacitances and forces in cylindrical systems,” (2018), arXiv:1801.08202 [physics.class-ph].
- [21] J. Lekner, *Electrostatics of conducting cylinders and spheres*, Vol. 22 (AIP Publishing, America, 2021).
- [22] R. Beals and J. Szmigielski, *Notices of the AMS* **60**, 866 (2013).
- [23] R. F. Harrington, “Field computation by moment methods,” (Wiley-IEEE Press, 1993) pp. 30–31.
- [24] H. B. Dwight and R. H. Romer, “Tables of integrals and other mathematical data,” (1988).